ACSNANO

www.acsnano.org

ARTICLE

Topological Hall Signatures of Two Chiral Spin Textures Hosted in a Single Tetragonal Inverse Heusler Thin Film

Pranava K. Sivakumar, Börge Göbel, Edouard Lesne, Anastasios Markou, Jyotsna Gidugu, James M. Taylor, Hakan Deniz, Jagannath Jena, Claudia Felser, Ingrid Mertig, and Stuart S. P. Parkin*

Cite This: *ACS Nano* 2020, 14, 13463−13469

Read Online

ACCESS | Metrics & More | Article Recommendations | Supporting Information

ABSTRACT: **Magnetic skyrmions and antiskyrmions are observed in material classes with different crystal symmetries, where the Dzyaloshinskii−Moriya interaction stabilizes either skyrmions or antiskyrmions. Here, we report the observation of two distinct peaks in the topological Hall effect in a thin film of Mn_2RhSn. Utilizing a phenomenological approach and electronic transport simulations, these topological Hall effect features are attributed to be direct signatures of two topologically distinct chiral spin objects, namely, skyrmions and antiskyrmions. Topological Hall effect studies allow us to determine the existence of these two topological objects over a wide range of temperature and magnetic fields. In particular, we find skyrmions to be stable at low temperatures, suggesting the increased importance of dipolar interactions.**

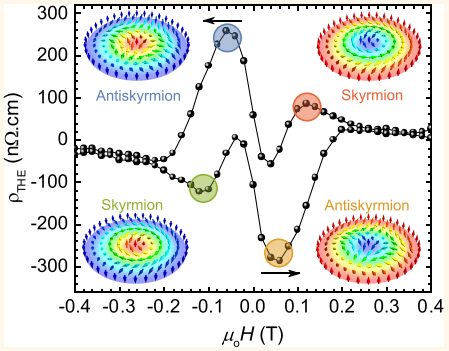

KEYWORDS: *skyrmions, antiskyrmions, topological Hall effect, noncollinear spin textures, inverse Heusler thin films*

Magnetic skyrmions[1−3] and antiskyrmions[4] are mesoscopic quasiparticles which are regarded as promising candidates for information recording in prospective future storage devices such as the racetrack memory.[5,6] They are typically observed in materials with distinct symmetries of the Dzyaloshinskii−Moriya exchange interaction (DMI).[7,8] In materials with D_{2d} symmetry, the anisotropic DMI stabilizes antiskyrmions, as first observed in the inverse Heusler system $Mn_{1.4}Pt_{0.9}Pd_{0.1}Sn$,[4] whereas in materials with cubic symmetry, such as MnSi and $Fe_{1-x}Co_xSi$, the isotropic DMI favors the occurrence of skyrmions.[1,2] Antiskyrmions are considered advantageous for racetrack applications, as it is expected that they can be driven without the hampering skyrmion Hall effect[9] that is inherently present for skyrmions.[10,11] Furthermore, the recent real-space observation of elliptical skyrmions with topological charges opposite to those of antiskyrmions was reported for $Mn_{1.4}Pt_{0.9}Pd_{0.1}Sn$ at low temperatures.[12] This observation, pointing toward the strengthening of magnetic dipolar interactions with decreasing temperatures, makes the class of D_{2d} materials distinct from, for example, cubic B20 materials, where the dipole−dipole interaction plays a less significant role.[12]

The nontrivial real-space topology in chiral objects can lead to emergent electrodynamic effects in the system, in particular, the topological Hall effect (THE).[13] When the interaction between electron spins and the topological spin texture is strong, the electron spin aligns locally with the texture so that a Berry phase is accumulated, leading to a transverse deflection of the electrons and the emergence of a topological Hall resistivity.[14] This effect has been observed in a variety of magnetic systems, including antiferromagnets with noncoplanar moments,[15] as well as in systems hosting skyrmions.[14,16] The THE arising from magnetic (anti)skyrmions is the focus of this paper.

In this study, we report Hall resistivity measurements of a sputtered thin film of Mn_2RhSn, an inverse Heusler compound with D_{2d} symmetry that is expected to host antiskyrmions.[4,17,18] We find that the THE displays a double-peaked feature as the field is swept from positive to negative magnetic fields, which is inverted as the field is swept in the opposite direction. We interpret these two features in terms of two topologically distinct phases present in the system: skyrmions and antiskyrmions. This interpretation is further supported by

Received: June 30, 2020
Accepted: September 28, 2020
Published: September 28, 2020

https://dx.doi.org/10.1021/acsnano.0c05413
ACS Nano 2020, 14, 13463−13469

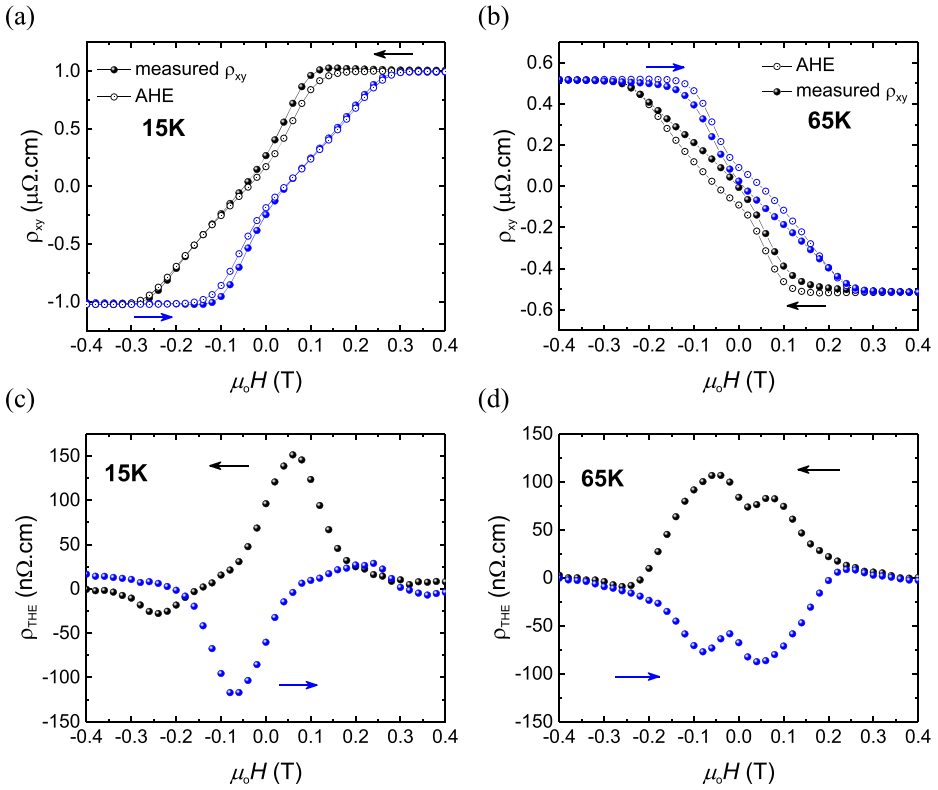

Figure 1. Topological Hall effect evolution in Mn_2RhSn. Measured Hall signal after subtracting the linear OHE (filled circles) superimposed on the calculated AHE (open circles) obtained by scaling the magnetization at (a) 15 K and (b) 65 K (arrows indicate field sweep directions; black color represents down-sweep, and blue color represents up-sweep). (c) At l5 K, the THE shows a strong single peak indicating the presence of a single topological phase. (d) Above 65 K, a clear separation of two peaks in the THE hysteresis signals the presence of two distinct topological phases (skyrmions and antiskyrmions) in the system (arrows indicate field sweep directions).

model electronic transport calculations of the topological Hall resistance originating from these two chiral spin textures.

Mn_2RhSn thin films were deposited using magnetron sputtering on MgO(001) single crystal substrates. The lattice mismatch between MgO(001) and Mn_2RhSn is only ~1.17%, resulting in the epitaxial growth of a (001) oriented thin film. We subsequently performed measurements of the Hall resistivity and magnetization of a 60 nm thick film as a function of the out-of-plane magnetic field along the [001] crystal axis.

We consider three additive effects that contribute to the Hall resistivity of our system. First is the ordinary Hall effect (OHE) which scales linearly with the magnetic field. Second is the anomalous Hall effect (AHE) which typically arises due to time reversal symmetry breaking in the ferromagnet and scales as the magnetization of the sample. The third effect is the THE, which occurs in a specific field range below magnetic saturation due to the presence of topologically nontrivial spin textures like skyrmions or antiskyrmions and is proportional to the average topological charge density of the spin textures present.[13,14] Thus, the total Hall resistivity can be described by

$$\rho_{xy} = R_0\mu_0 H + R_S M(\mu_0 H) + \rho_{\mathrm{THE}} \quad (1)$$

where R_0 is the ordinary Hall coefficient; R_S is the AHE coefficient; $M(\mu_0 H)$ is the out-of-plane magnetization of the thin film as a function of the applied magnetic field ($\mu_0 H$), and ρ_{THE} is the topological Hall resistivity of the sample. Therefore, the THE can be obtained by subtracting the other two contributions from the measured Hall signal.

RESULTS AND DISCUSSION

Hall Resistivity Measurements and Observation of Pure Topological Hall Signal. Figure 1a,b displays the Hall resistivity (ρ_{xy}) measured at two different temperatures after subtracting the linear contribution of the OHE. In the Supporting Information, we present the raw data and details of the fitting procedures that were used. The OHE, which is linear, is subtracted by fitting a linear function above 1 T. There is a small nonlinear background that is observed at low fields while removing the OHE. Possible reasons for this background could be a planar Hall contribution due to a very small tilt in the sample with respect to the field or a nonzero contribution from linear magnetoresistance. After subtracting the OHE contribution, the AHE is removed by superimposing the data on the anticipated contribution. This expected contribution to the AHE is obtained by scaling the out-of-plane magnetization of the sample (M_z) to the values corresponding to ±0.36 T of the measured ρ_{xy} data after removing the OHE. The ρ_{THE} contribution after subtracting the OHE and AHE is shown in Figure 1c,d. At low temperatures (15 K; see Figure 1c), a large peak is observed, around ±0.05 T, well below the saturation magnetic field, as is typically the case with (anti)skyrmions.[14,16,19] This peak can therefore be attributed to the presence of either skyrmions or antiskyrmions, which have already been observed in inverse Heusler compounds.[4,12] A second, much smaller negative peak is found in opposite fields (around ∓0.24T) of the same hysteresis branch, pointing toward the stability of the same topologically nontrivial object in an oppositely magnetized

https://dx.doi.org/10.1021/acsnano.0c05413
ACS Nano 2020, 14, 13463−13469

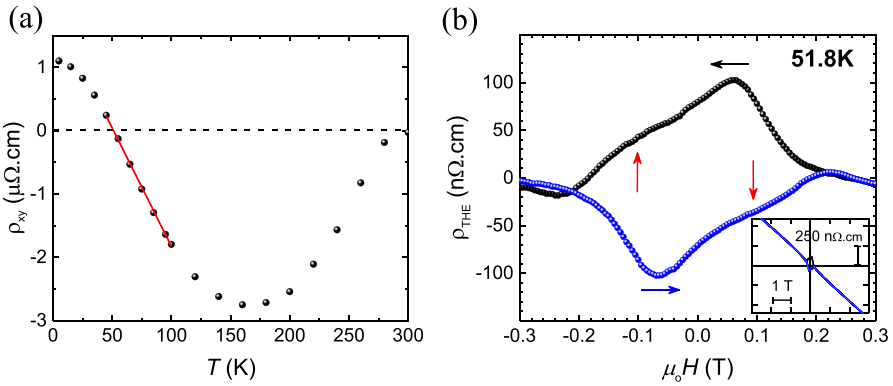

Figure 2. Pure topological Hall effect at compensation temperature. (a) Temperature dependence of the anomalous Hall resistivity which passes through zero at a temperature of 51.8 K. The dashed black line indicates zero AHE, and the red line is a linear fit used to precisely locate the temperature at which the AHE passes through zero. (b) Pure THE measured at 51.8 K after subtraction of solely the linear OHE (blue and black arrows indicate field sweep directions). The regular THE peak can be seen accompanied by a wide shoulder in both branches of the hysteresis loop (marked with vertical red arrows), indicating the nucleation of a second topological phase in the system. The inset displays the measured Hall resistivity at 51.8 K, before subtracting the linear OHE, clearly showing the absence of an AHE.

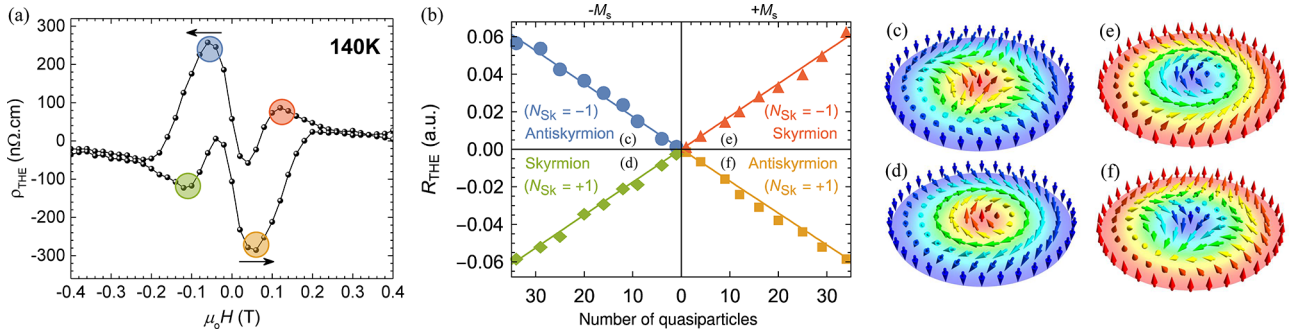

Figure 3. Emergence of skyrmions and antiskyrmions. (a) Measured topological Hall resistivity at 140 K. The two peaks per hysteresis branch correspond to two distinct magnetic phases with the same topological charge. As the peaks occur for magnetization of different signs, the origin can be attributed to skyrmions and antiskyrmions formed in oppositely magnetized surroundings. (b) Electronic transport simulations of the topological Hall resistance for $+M_S$ or $-M_S$ magnetized samples (151 × 151 sites) with randomly positioned skyrmions or antiskyrmions. The calculated signal is proportional to $\langle N_{Sk} \rangle$, allowing for correlation of the four peaks from (a) (marked with different colors) to the four different magnetic textures, depicted in (c–f). The Fermi energy is chosen to be E_F = 1.24 eV to model free electrons.

sample. The smaller magnitude of this peak implies that fewer of such objects form in this case.

When the same measurement is carried out at 65 K (Figure 1b), certain qualitative differences in the Hall resistivity become apparent, as shown in Figure 1d. First, the anomalous Hall resistivity, which is positive at lower temperatures, decreases linearly with increasing temperature and changes sign, indicating a strong temperature dependence of the AHE coefficient R_S. Second, the small THE peak vanishes into the background. Third, the THE evolves a shoulder that, with increasing temperature, splits into two prominent peaks, with the same sign as the main peak, in both the positive to negative (down-sweep) and negative to positive (up-sweep) magnetic field hysteresis branches. For each down-sweep, the peak which occurs at positive fields at low temperatures is referred to as the first peak, and the other peak which nucleates above 65 K and occurs at negative fields is referred to as the second peak.

Upon increasing the temperature, the AHE changes sign from positive to negative around 51.8 K, as shown in Figure 2a. Therefore, measuring the Hall resistivity at this particular temperature where the AHE contribution vanishes allows an unambiguous measurement of the THE, without the need to further calculate and subtract the AHE from the raw data. In Figure 2b, ρ_{xy} is plotted at 51.8 K after solely subtracting the linear OHE contribution, which evidences the nucleation of the second THE feature. One main peak is accompanied by a shoulder at negative magnetic field (in the case of down-sweep), and as the temperature is increased further, this shoulder-like feature is seen to evolve into the second peak observed at higher temperatures as shown in Figure 3a for 140 K.

Phenomenological Origin of the Double-Peaked THE Feature: Emergence of Skyrmions and Antiskyrmions. Using a phenomenological model, we explain the origin of the double-peak feature in THE by the presence of both skyrmions and antiskyrmions. The topological Hall resistivity is proportional to the average topological charge density:[14,20]

$$\rho_{THE} = R_T \langle N_{Sk} \rangle \quad (2)$$

where $\langle N_{Sk} \rangle$ is the total topological charge, that is, the sum of the topological charges, N_{Sk}, of all individual objects present. The topological Hall coefficient, R_T, which is determined by the carrier density and the spin polarization of the carriers, condenses the properties of the band structure. A sign change of this coefficient is only conceivable when the temperature is varied but not upon tuning the external field as this leaves the carrier densities invariant. For this reason, the sign of the two peaks in the topological Hall resistivity indicates two distinct

https://dx.doi.org/10.1021/acsnano.0c05413
ACS Nano 2020, 14, 13463−13469

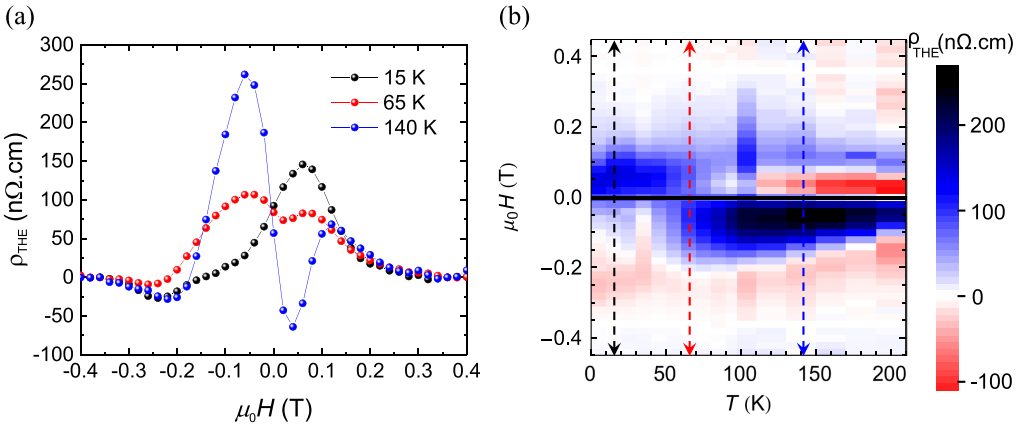

Figure 4. Temperature and field dependence of the topological Hall effect. (a) Isolated topological contribution to the Hall resistivity for three selected temperatures (15, 65, and 140 K), visualizing how the magnitudes of the two peaks evolve with temperature. (b) Map of temperature and field dependence for the down-sweep is shown. Dashed lines of different colors correspond to the curves in (a).

topological phases and can be related directly to the topological charges of the objects.

It is essential to keep in mind that the topological charge of (anti)skyrmions (N_{sk}) is not solely determined by the winding direction of the magnetic texture. This refers to a quantity called vorticity ($m = +1$ for a skyrmion and $m = -1$ for an antiskyrmion) and has to be multiplied by the polarity of the (anti)skyrmion for the determination of the topological charge.[13,21]

$$N_{sk} = mp = \pm 1 \tag{3}$$

The polarity p characterizes the out-of-plane orientation of the core magnetic moment of a skyrmion or an antiskyrmion, which is determined by the magnetization background, that is, $p = +1$ in a $-M_S$ magnetized sample, whereas $p = -1$ in a $+M_S$ magnetized sample. The four different possible combinations of m and p for (anti)skyrmionic textures are shown in Figure 3c–f. In particular, this means that skyrmions and antiskyrmions in oppositely magnetized samples are characterized by the same topological charge.

In our measurements, as both peaks in a single hysteresis branch have the same sign, the topological charges of both the objects can be inferred to be of the same sign, as well. However, as the second peak always appears at fields with magnitudes larger than the coercive field, at which the magnetization of the sample has reversed its direction (refer to Figure S8), the sample magnetization for which the two THE peaks occur is opposite in sign, implying opposite polarities $p = \pm 1$ for the two topological quasiparticles present in a single hysteresis branch. This leads to the inference that the vorticities of the two topological phases present must also be opposite: $m = \pm 1$. In other words, the two features correspond to skyrmions and antiskyrmions in an oppositely magnetized sample.

We contrast our results and phenomenological explanation with the THE observed due to skyrmions in Ir/Fe/Co/Pt multilayers.[20] In this work, THE of opposite signs are observed due to skyrmions occurring in oppositely magnetized backgrounds. This result from the literature reinforces our phenomenological explanation and the need for occurrence of antiskyrmions to explain the occurrence of two peaks of the same sign in oppositely magnetized backgrounds. It is also to be noted that even the deformed skyrmionic worms have the same sign of THE as regular skyrmions, indicating that the polarity of the skyrmions remains unchanged.

Electronic Transport Model Simulations. The above phenomenological explanation for the observation of the two-featured THE is validated by electronic transport simulations. For each of the four combinations of skyrmions and antiskyrmions, both with two possible polarities, we consider a fixed number of randomly positioned objects, all of one kind, in a square shaped area (refer to the Methods section for details).

In the adiabatic limit, the simulations result in a transverse deflection of electrons toward the detecting leads and the emergence of a topological Hall resistivity. As apparent from Figure 3b, this phenomenological approach is indeed a valid approximation: the topological Hall resistivity is solely proportional to the total topological charge in the system (small deviations occur due to the random placement of the magnetic quasiparticles—an effect that would decrease for larger simulated sample sizes). This allows us to relate the two peaks in the THE to the presence of skyrmions and antiskyrmions in oppositely magnetized phases (the four peaks indicated by different colors in Figure 3a correspond to the color scheme of Figure 3b). Furthermore, the different magnitudes of the measured peaks can be related to different number densities of skyrmions and antiskyrmions in the two phases. In the Supporting Information, we show that this is valid over a large range of parameters used in the simulation.

Temperature and Magnetic Field Evolution of the Topological Hall Effect. To explore the relative distribution of the two topological objects, we further investigate the variation in magnitude of the two peaks in the measured THE as a function of temperature and magnetic field. In Figure 4a, the extracted topological contribution to the Hall resistivity is shown for the down-sweeps at three different temperatures. As already indicated in Figure 1c, at low temperatures (black), only one peak is present when the magnetic field is decreased from the field-polarized state. Upon increasing the temperature, the magnitude of this peak decreases but a second feature increases in magnitude until it surpasses the signal of the low-temperature THE feature at around 65 K (red). As the temperature is increased further to 140 K (blue), the second feature becomes much more prominent.

The measurement of the topological Hall resistivity in the down-sweep of the hysteresis for an extended range of

https://dx.doi.org/10.1021/acsnano.0c05413
ACS Nano 2020, 14, 13463−13469

temperatures and magnetic fields is plotted as a phase diagram in Figure 4b. The first feature of the THE can be seen as a blue area which predominantly occurs at lower temperatures and small positive magnetic fields which monotonically decline in magnitude with increasing temperature. Meanwhile, the second feature can be seen as a large dark-blue patch occurring at negative fields and over a wide range of elevated temperatures (predominantly above 55 K) that increases in magnitude with increasing temperature.

Our electrical transport measurements and theoretical calculations indicate that two topologically distinct phases are present in Mn_2RhSn thin films, which we interpret in terms of skyrmions and antiskyrmions. The presence of two peaks in the topological Hall resistivity, one stronger at low temperatures and the other at higher temperatures, indicates that the two distinct chiral objects are stabilized by competing interactions, whose strength is dependent on the temperature.

In agreement with Lorentz transmission electron microscopy imaging carried out on crystals of a similar D_{2d} system ($Mn_{1.4}Pt_{0.9}Pd_{0.1}Sn$) and the micromagnetic simulations presented in another study,[12] we attribute the first THE peak, found at lower temperatures, to the occurrence of skyrmions. Even though the D_{2d} symmetry of Mn_2RhSn induces an anisotropic DMI, which stabilizes antiskyrmions in the framework of our interpretation, the dipole−dipole interaction becomes dominant at lower temperatures, allowing for the stabilization of skyrmions. As M decreases monotonically with increasing temperatures (as shown in Figure S4), the relevance of the dipolar interactions also decays, which leads to a decrease in the skyrmion number density. This inference is in accordance with the observed trend of the magnitude of the first THE peak decreasing with temperature.

Having established the first THE peak to the formation of skyrmions, we can attribute the second THE peak, according to our model, to the formation of antiskyrmions. The antiskyrmions, which are stabilized by the anisotropic DMI, are found to occur predominantly at higher temperatures where the relevance of the dipole−dipole interaction is reduced. In agreement with our predictions, we observe that, at low temperatures, the skyrmion peak extends down to and beyond zero field, whereas for elevated temperatures, the antiskyrmion peak is the one that extends to zero field. Both of these nano-objects are stable in their favorable temperature ranges.

Our results are consistent with theoretical predictions for skyrmions and antiskyrmions in D_{2d} materials as well as their real-space observation, using Lorentz transmission electron microscopy, in crystals of $Mn_{1.4}Pt_{0.9}Pd_{0.1}Sn$.[12] We find that in Mn_2RhSn, a material which belongs to the same D_{2d} symmetry group, the skyrmion phase becomes the more stable one at much lower temperatures. The increased stability of these noncollinear objects in films of Mn_2RhSn is in analogy with thin films of B20 materials, where the stable field and temperature range for the stabilization of the skyrmion lattice phase are drastically increased compared to bulk samples.[16] In a previous study of the same material,[18] which is limited to positive magnetic fields, a positive THE has been observed from 2 to 100 K with decreasing magnitude. This feature is the one that we identify as being due to skyrmions rather than antiskyrmions. We attribute the difference in trends of AHE, as compared to the previous study,[18] to a variation in the actual composition of the films. While comparing the growth conditions, we use a growth temperature (400 °C) slightly higher than that of the previous study (350 °C).[18] The composition of the film used in this study as obtained from EDAX (Mn/Rh/Sn = 51.2:24.3:24.5) is closer to the 2:1:1 ratio compared to that in the previous study (Mn/Rh/Sn = 52.6:21.7:25.6).[18] This difference in composition can introduce self-doping in the films, which can shift the chemical potential of the films, leading to a variation in the observed AHE.

CONCLUSION

In summary, we have identified two distinct features in the topological Hall resistivity of a thin film of Mn_2RhSn, which we attribute to the existence of a skyrmion and an antiskyrmion phase stabilized at different temperatures due to differing strengths of dipolar interactions and anisotropic DMI, respectively. There is also a considerable intermediate temperature range in which the two phases are found to coexist. Thin films of Mn_2RhSn are thus favorable systems to realize the coexistence of skyrmions and antiskyrmions at the same temperature, potentially offering controlled switching between the two states through tuning of the magnetic field. Our observation of these topological magneto-transport properties in thin films and understanding their origin help in accelerating the development of skyrmion- and antiskyrmion-based spintronic devices. For instance, the coexistence of skyrmions and antiskyrmions allows us to envision a racetrack storage device in which the two chiral objects can act as the two logical states of a bit of information. Such a device would allow for irregular bit sequences, as they are encoded by distinct nano-objects and would be less susceptible to thermal fluctuations and attractive interactions.

METHODS

Thin Film Growth. The Mn_2RhSn film with a thickness of 60 nm was grown heteroepitaxially on a MgO(001) single crystal substrate. A BESTEC UHV magnetron sputtering system was used for the deposition of the film, with Mn, Rh, and Sn sources in a confocal geometry. The target to substrate distance was 20 cm. Prior to deposition, the chamber was evacuated to a base pressure less than 2×10^{-9} mbar, whereas the process gas (Ar 5N) pressure was 3×10^{-3} mbar. The Mn_2RhSn film was grown by co-sputtering, and the individual sputter rates were adjusted to obtain the desired composition. Mn was deposited by applying 27 W DC power, Rh by applying 20 W DC power, and Sn by applying 11 W DC, and the total rate was 0.73 Å/s. The substrate was rotated at 20 rpm during deposition to ensure homogeneous growth. The film was grown at 400 °C and then postannealed *in situ* for an additional 30 minutes to improve chemical ordering. The sample was capped with a 3 nm thick Al film at room temperature to prevent oxidation. This ultrathin aluminum naturally passivates in air to form insulating aluminum oxide. By means of ultrasonic wire-bonding, we penetrate through this layer and make contact with the Heusler film. Stoichiometry was estimated as $Mn_{51}Rh_{24}Sn_{25}$ by energy-dispersive X-ray spectroscopy with an experimental uncertainty of ±2%. X-ray diffraction (XRD) and X-ray reflectivity (XRR) were measured with a Panalytical X'Pert3 MRD diffractometer, using Cu Kα1 radiation (λ = 1.5406 Å). The growth rates and film thicknesses were determined by a quartz crystal microbalance and confirmed through XRR measurements.

Structural Analysis. Additional XRD measurements, $2\theta-\omega$ scans, and sample azimuth (ϕ) scans were performed to study the structure, the crystallinity, and the heteroepitaxial relationship between the film and the substrate. The in-plane lattice mismatch between the MgO substrate and bulk Mn_2RhSn is 1.17%, which allows the heteroepitaxial growth of a (001) oriented film. The XRD pattern of a 60 nm Mn_2RhSn film is shown in Figure S1a. Only the (002) and (004) reflections of the tetragonal Mn_2RhSn are observed, indicating

https://dx.doi.org/10.1021/acsnano.0c05413
ACS Nano 2020, 14, 13463−13469

that the samples are (001) oriented. Combining the peak positions of the (004) reflection and the partially in-plane (112) reflection, the lattice parameters of Mn_2RhSn are calculated to be $a = b = 4.346$ Å and $c = 6.472$ Å.

High-angle annular dark-field scanning transmission electron microscope images were acquired using an FEI TITAN 80-300 electron microscope operated at 300 kV (Figure S3). An electron transparent lamella for transmission electron microscopy observation was prepared using Ga ions in a focused ion beam system. An enlarged cut-out image (Figure S3b) from the film region was obtained after applying Wiener and Butterworth filters in Fourier space to remove the contribution due to amorphous background and to eliminate high-frequency noise components, respectively.

Magnetization Measurements. The magnetization of the sample at various temperatures was measured in a Quantum Design MPMS3 SQUID magnetometer. Magnetic field sweeps were carried out between +2 and −2 T. The diamagnetic contribution to the signal arising from the MgO substrate was removed by subtracting the magnetization recorded in a reference measurement of an MgO substrate with similar dimensions.

Electrical Transport Measurements. Hall measurements at different temperatures were performed on a 2 mm by 2 mm sample using a four-point probe method in the Van der Pauw geometry, as shown in Figure S6e. The measurements were performed in a Quantum Design PPMS using a Keithley 6221 current source to supply direct currents of density 6×10^6 Am^{-2}, and the voltage signals were detected using a Keithley 2182A nanovoltmeter. Magnetic field sweeps were done between +4 and −4 T, with the sample plane perpendicular to the magnetic field. The ordinary Hall effect, which is linear in field, is subtracted from the data by performing a linear fit of the high field regime (between 1 and 4 T), where the anomalous Hall resistivity saturates and the topological contribution to the Hall effect is zero. The AHE, which is proportional to the magnetization of the sample, is subtracted by scaling the measured magnetization loops such that the saturation magnetization matches the magnitude of the AHE signal just above the saturation field (±0.36 T).

Electronic Transport Simulations. The aim of these calculations is to confirm eq 2. For simplicity, a single orbital hopping model ($c_i^\dagger$ creation operator, c_i annihilation operator of an electron at site i)

$$H = \sum_{\langle i,j \rangle} t c_i^\dagger c_j + m \sum_i \boldsymbol{s}_i \cdot (c_i^\dagger \boldsymbol{\sigma} c_i) \tag{4}$$

on a square lattice is used, yielding a band structure of $E = 2t[\cos(k_x a) + \cos(k_y a)] \pm m$ for a collinear ferromagnet. Here, t is the hopping amplitude of nearest neighbors $\langle i,j \rangle$, and m quantifies the Hund's coupling of the electron spins ($\boldsymbol{\sigma}$ is the vector of Pauli matrices) and the magnetic texture $\{\boldsymbol{s}_i\}_i$. The adiabatic limit has been simulated using $t = 1$ eV, $m = 5$ eV. Spin−orbit coupling has been disregarded to isolate the topological Hall contribution. To simulate the effect of topologically nontrivial spin textures, skyrmions ($m = 1$) or antiskyrmions ($m = -1$) with a profile

$$s_i^{(z)}(r_i) = \begin{pmatrix} \frac{y}{r}\sin(\pi r_i/20a) \\ -m\frac{x}{r}\sin(\pi r_i/20a) \\ \mp \cos(\pi r_i/20a) \end{pmatrix}$$

have been positioned randomly in a $+M_S$ or $-M_S$ magnetized sample, respectively.

To model the current and the charge accumulation, four semi-infinite terminals are added at the four sides of the simulated sample. A current is injected from the left terminal to the right ($I = I_{left} = -I_{right}$) and the voltage between the top (U_{top}) and the bottom (U_{bottom}) terminal is calculated using a Landauer−Büttiker approach. These quantities determine the resistance, $R_{xy} = (U_{top} - U_{bottom})/I$, which gives the resistivity ρ_{xy}. The voltages U_n and currents I_m at the four leads are related linearly $I_m = e^2/hT_{mn}U_n$ by the transition matrix T that has been calculated using the code Kwant[22] in analogy with ref 23. The Supporting Information contains Figure S9, which is an overview of the considered geometry and Figures S10 and S11 which show that the results do not qualitatively depend on the Hund's coupling parameter m.

ASSOCIATED CONTENT

Supporting Information

The Supporting Information is available free of charge at https://pubs.acs.org/doi/10.1021/acsnano.0c05413.

Details of structural characterizations using XRD and HR-STEM, electrical and magnetic measurements, step-by-step extraction and error analysis of the THE along with associated details of the transport simulation (PDF)

AUTHOR INFORMATION

Corresponding Author

Stuart S. P. Parkin − *Max Planck Institute of Microstructure Physics, 06120 Halle, Germany;* orcid.org/0000-0003-4702-6139; Email: stuart.parkin@mpi-halle.mpg.de

Authors

Pranava K. Sivakumar − *Max Planck Institute of Microstructure Physics, 06120 Halle, Germany*

Börge Göbel − *Max Planck Institute of Microstructure Physics, 06120 Halle, Germany; Institute of Physics, Martin Luther University Halle-Wittenberg, 06099 Halle, Germany;* orcid.org/0000-0003-4050-6869

Edouard Lesne − *Max Planck Institute of Microstructure Physics, 06120 Halle, Germany*

Anastasios Markou − *Max Planck Institute for Chemical Physics of Solids, 01187 Dresden, Germany*

Jyotsna Gidugu − *Max Planck Institute of Microstructure Physics, 06120 Halle, Germany*

James M. Taylor − *Max Planck Institute of Microstructure Physics, 06120 Halle, Germany;* orcid.org/0000-0001-5274-8545

Hakan Deniz − *Max Planck Institute of Microstructure Physics, 06120 Halle, Germany*

Jagannath Jena − *Max Planck Institute of Microstructure Physics, 06120 Halle, Germany*

Claudia Felser − *Max Planck Institute for Chemical Physics of Solids, 01187 Dresden, Germany*

Ingrid Mertig − *Institute of Physics, Martin Luther University Halle-Wittenberg, 06099 Halle, Germany*

Complete contact information is available at: https://pubs.acs.org/10.1021/acsnano.0c05413

Notes

The authors declare no competing financial interest.

ACKNOWLEDGMENTS

P.K.S. and E.L. would like to thank K.G. Rana for fruitful discussions. B.G. and I.M. acknowledge funding by the Deutsche Forschungsgemeinschaft (DFG, German Research Foundation) under SFB TRR 227. Funding by the Deutsche Forschungsgemeinschaft (DFG, German Research Foundation) under SPP 2137 is acknowledged by C.F. and A.M. (Project No. 403502666) and S.S.P.P. (Project No. 403505322).

REFERENCES

(1) Mühlbauer, S.; Binz, B.; Jonietz, F.; Pfleiderer, C.; Rosch, A.; Neubauer, A.; Georgii, R.; Böni, P. Skyrmion Lattice in a Chiral Magnet. *Science* **2009**, *323*, 915−919.

(2) Yu, X. Z.; Onose, Y.; Kanazawa, N.; Park, J. H.; Han, J. H.; Matsui, Y.; Nagaosa, N.; Tokura, Y. Real-Space Observation of a Two-Dimensional Skyrmion Crystal. *Nature* **2010**, *465*, 901−904.

(3) Heinze, S.; Von Bergmann, K.; Menzel, M.; Brede, J.; Kubetzka, A.; Wiesendanger, R.; Bihlmayer, G.; Blügel, S. Spontaneous Atomic-Scale Magnetic Skyrmion Lattice in Two Dimensions. *Nat. Phys.* **2011**, *7*, 713−718.

(4) Nayak, A. K.; Kumar, V.; Ma, T.; Werner, P.; Pippel, E.; Sahoo, R.; Damay, F.; Rößler, U. K.; Felser, C.; Parkin, S. S. P. Magnetic Antiskyrmions above Room Temperature in Tetragonal Heusler Materials. *Nature* **2017**, *548*, 561−566.

(5) Parkin, S. S. P.; Hayashi, M.; Thomas, L. Magnetic Domain-Wall Racetrack Memory. *Science* **2008**, *320*, 190−194.

(6) Fert, A.; Cros, V.; Sampaio, J. Skyrmions on the Track. *Nat. Nanotechnol.* **2013**, *8*, 152−156.

(7) Dzyaloshinsky, I. A. Thermodynamic Theory of "Weak" Ferromagnetism of Antiferromagnetics. *J. Phys. Chem. Solids* **1958**, *4*, 241−255.

(8) Moriya, T. Anisotropic Superexchange Interaction and Weak Ferromagnetism. *Phys. Rev.* **1960**, *120*, 91−98.

(9) Huang, S.; Zhou, C.; Chen, G.; Shen, H.; Schmid, A. K.; Liu, K.; Wu, Y. Stabilization and Current-Induced Motion of Antiskyrmion in the Presence of Anisotropic Dzyaloshinskii-Moriya Interaction. *Phys. Rev. B: Condens. Matter Mater. Phys.* **2017**, *96*, 144412.

(10) Litzius, K.; Lemesh, I.; Krüger, B.; Bassirian, P.; Caretta, L.; Richter, K.; Büttner, F.; Sato, K.; Tretiakov, O. A.; Förster, J.; Reeve, R. M.; Weigand, M.; Bykova, I.; Stoll, H.; Schütz, G.; Beach, G. S. D.; Klaüi, M. Skyrmion Hall Effect Revealed by Direct Time-Resolved X-Ray Microscopy. *Nat. Phys.* **2017**, *13*, 170−175.

(11) Jiang, W.; Zhang, X.; Yu, G.; Zhang, W.; Wang, X.; Benjamin Jungfleisch, M.; Pearson, J. E.; Cheng, X.; Heinonen, O.; Wang, K. L.; Zhou, Y.; Hoffmann, A.; Te Velthuis, S. G. E. Direct Observation of the Skyrmion Hall Effect. *Nat. Phys.* **2017**, *13*, 162−169.

(12) Jena, J.; Göbel, B.; Ma, T.; Kumar, V.; Saha, R.; Mertig, I.; Felser, C.; Parkin, S. S. P. Elliptical Bloch Skyrmion Chiral Twins in an Antiskyrmion System. *Nat. Commun.* **2020**, *11*, 1115.

(13) Nagaosa, N.; Tokura, Y. Topological Properties and Dynamics of Magnetic Skyrmions. *Nat. Nanotechnol.* **2013**, *8*, 899−911.

(14) Neubauer, A.; Pfleiderer, C.; Binz, B.; Rosch, A.; Ritz, R.; Niklowitz, P. G.; Böni, P. Topological Hall Effect in the a Phase of MnSi. *Phys. Rev. Lett.* **2009**, *102*, 186602.

(15) Sürgers, C.; Fischer, G.; Winkel, P.; Löhneysen, H. V. Large Topological Hall Effect in the Non-Collinear Phase of an Antiferromagnet. *Nat. Commun.* **2014**, *5*, 3400.

(16) Li, Y.; Kanazawa, N.; Yu, X. Z.; Tsukazaki, A.; Kawasaki, M.; Ichikawa, M.; Jin, X. F.; Kagawa, F.; Tokura, Y. Robust Formation of Skyrmions and Topological Hall Effect Anomaly in Epitaxial Thin Films of MnSi. *Phys. Rev. Lett.* **2013**, *110*, 117202.

(17) Meshcheriakova, O.; Chadov, S.; Nayak, A. K.; Rößler, U. K.; Kübler, J.; André, G.; Tsirlin, A. A.; Kiss, J.; Hausdorf, S.; Kalache, A.; Schnelle, W.; Nicklas, M.; Felser, C. Large Noncollinearity and Spin Reorientation in the Novel Mn_2RhSn Heusler Magnet. *Phys. Rev. Lett.* **2014**, *113*, 087203.

(18) Rana, K. G.; Meshcheriakova, O.; Kübler, J.; Ernst, B.; Karel, J.; Hillebrand, R.; Pippel, E.; Werner, P.; Nayak, A. K.; Felser, C.; Parkin, S. S. P. Observation of Topological Hall Effect in Mn_2RhSn Films. *New J. Phys.* **2016**, *18*, 085007.

(19) Swekis, P.; Markou, A.; Kriegner, D.; Gayles, J.; Schlitz, R.; Schnelle, W.; Goennenwein, S. T. B.; Felser, C. Topological Hall Effect in Thin Films of $Mn_{1.5}PtSn$. *Phys. Rev. Mater.* **2019**, *3*, 013001.

(20) Raju, M.; Yagil, A.; Soumyanarayanan, A.; Tan, A. K. C.; Almoalem, A.; Ma, F.; Auslaender, O. M.; Panagopoulos, C. The Evolution of Skyrmions in Ir/Fe/Co/Pt Multilayers and Their Topological Hall Signature. *Nat. Commun.* **2019**, *10*, 696.

(21) Kovalev, A. A.; Sandhoefner, S. Skyrmions and Antiskyrmions in Quasi-Two-Dimensional Magnets. *Front. Phys.* **2018**, *6*, 98.

(22) Groth, C. W.; Wimmer, M.; Akhmerov, A. R.; Waintal, X. Kwant: A Software Package for Quantum Transport. *New J. Phys.* **2014**, *16*, 063065.

(23) Göbel, B.; Schäffer, A. F.; Berakdar, J.; Mertig, I.; Parkin, S. S. P. Electrical Writing, Deleting, Reading, and Moving of Magnetic Skyrmioniums in a Racetrack Device. *Sci. Rep.* **2019**, *9*, 12119.

https://dx.doi.org/10.1021/acsnano.0c05413
ACS Nano 2020, 14, 13463−13469